

Research Article

Discrete Prediction of Grain Evolution in Solid-State Welding of Ti₆Al₄-V Alloy

Johana Gamez ^{ID}, David Briones, Carlos Garza ^{ID}, Yadira Gonzalez, Maria Nañez, Patricia Zambrano-Robledo ^{ID}, Luis A. Reyes ^{*ID}

School of Mechanical and Electrical Engineering, Autonomous University of Nuevo Leon, Nuevo Leon, Mexico
E-mail: luis.reyessr@uanl.edu.mx

Received: 7 September 2024; **Revised:** 20 November 2024; **Accepted:** 14 January 2025

Abstract: Titanium (Ti) alloys, known for their high strength and low weight, are essential in aircraft and aerospace applications. This study focuses on friction spot welding as an innovative, efficient process that creates robust Ti alloys joints while minimizing the carbon footprint. The research aims to develop a cellular automata (CA) model to analyze grain evolution during the friction stir spot welding of Ti₆Al₄V alloy. The methodology involved simulating the welding process at rotational speeds ranging from 800 to 1,200 rpm using a complex curved-thread shoulder. The CA model incorporated both deterministic and probabilistic approaches to capture the dynamic recrystallization (DRX) behavior. Grain nucleation and growth were modeled based on dislocation density, allowing for an in-depth assessment of the alloy's microstructural changes driven by hardening and softening mechanisms. Validation was performed by comparing the model's predictions with experimental measurements of temperature and grain size. The findings indicate that heat and deformation during welding significantly influence grain size evolution, enhancing the understanding of microstructural behavior in high-strength titanium joints. This work contributes valuable insights into optimizing welding techniques for titanium alloys in aerospace engineering.

Keywords: friction stir spot welding, cellular automata, microstructure, Ti₆Al₄V alloy

MSC: 74S30, 82B26, 74N05

1. Introduction

Titanium alloys offer outstanding benefits due to their corrosion resistance, high strength and low weight. Examples of parts manufactured from titanium alloys include blades and discs for aircraft turbines, aircraft fuselages and automotive components [1]. Ti₆Al₄V is a heat-treatable titanium alloy composed of two phases ($\alpha + \beta$) with different microstructural morphologies. Ti₆Al₄V is one of the most widely used titanium alloys due to its good mechanical and thermal properties, excellent corrosion resistance and stability at elevated temperatures [2–4].

Fabrication of titanium structures often requires a welding process that produces sound joints while avoiding distortion and residual stresses. Friction stir welding (FSW) is an innovative welding process that has been proven successful in producing high-quality welds in Al and Ti alloys. This process was developed in Cambridge, UK, in 1991

[5]. FSW involves a rotating tool that creates cyclical motion between the joining plates, with heat generated through friction, causing the material to plasticize. As a variant of FSW, friction stir spot welding (FSSW) was developed to spot weld high-strength alloys [6]. The FSSW process serves as an alternative to traditional spot-welding techniques and is considered an efficient and environmentally friendly solution.

The principal parameters of FSSW are rotational speed, plunge velocity and plunge penetration [7]. The basic steps of the welding process include the immersion step, holding and retraction. During the immersion step, the rotating tool is gradually inserted into the workpiece. As this takes place, the cold material begins to flow and the rubbing action leads to the consolidation of the material [8]. The increase in temperature and the degree of plastic flow are associated with this immersion step [9]. The tool continues to penetrate until the tool shoulder is fully in contact with the workpieces. The heating of the workpieces results from friction and the applied axial force gradually decreases as the metal reaches the critical temperature for plastic flow [10]. After the immersion stage, the tool is intentionally held for a short period of time to reach the required temperature and allow for microstructural transformation. Finally, the retraction step occurs, during which the tool stops moving and is withdrawn from the workpiece. FSSW is frequently used to join complex materials such as titanium and high-strength steels [11]. The primary function of the welding tool is to heat the plates and facilitate material flow [12–15].

Frequently, FSSW results in four distinct regions: the agitation or stir zone (SZ), the thermo-mechanically affected zone (TMAZ), the heat-affected zone (HAZ) and the parent metal. The SZ is characterized by localized strain and high temperatures, while the TMAZ exhibits a distorted microstructure with elongated grains. Additionally, the HAZ only shows thermal gradients with a moderate strain effect [16]. Although there is substantial literature on FSW processing of complex alloys, a comprehensive understanding of FSSW remains limited [17].

Recently, diverse studies have been conducted to evaluate friction welding process via experimental and numerical methods. The impact of processing parameters, workpiece material and tool characteristics are usually investigated. Sarikavak [18] explored the thermal effects on FSW of high-strength alloys. A transient numerical model was developed to evaluate the temperature distribution during welding. The numerical model was compared with experimental results using steel, aluminum and titanium as tool materials. Su et al. [19] investigated the input parameters of FSW, such as friction coefficient and rotational velocity. Medhi et al. [20] created a numerical model to evaluate the thermal effect under diverse welding conditions using an Al alloy as a workpiece material. Zhang et al. [21] performed experiments to determine the influence of shoulder size on the temperature distribution.

In FSW, the temperature distribution and resulting material flow can be described using integral equations that may exhibit weak singular behavior due to several factors, such as localized heat generation and boundary effects. Traditional mathematical models, often based on classical differential equations, may fall short in capturing the intricacies of such highly dynamic systems. In this context, the use of fractional differential equations has emerged as an innovative approach for more accurately modeling the underlying processes [22, 23]. Volterra integral equations often model time-dependent phenomena such as transient heat conduction, while Fredholm integral equations can represent steady-state processes involving spatial domains [24, 25]. The incorporation of fractional terms into recrystallization models provides improved predictions of grain stability and size distribution across the stir zone.

In addition, discrete models, such as cellular automata (CA), enable the prediction of dynamic microstructure transformations during friction welding processes. The CA technique consists of an assembly of regular cells that are updated at each time step based on deterministic or predetermined values. Each cell in the domain is interconnected, and these connections govern how the cell evolves over time. The probabilistic framework of the CA model is established through random cell updates. The CA model uses dislocation density as a state variable to represent the kinetics of recrystallization [26]. The development of recrystallization (including nucleation and growth) is defined by a critical dislocation density.

Microstructure modeling using cellular automaton (CA) models has been explored recently. Pourian et al. [27] created a CA model to determine the microstructure evolution of an alpha Ti alloy. The CA model consisted of 900 cells randomly distributed to generate a non-textured microstructure. The stress vs. strain curves were compared and similar results were determined. Li et al. [28] developed a grain growth model using a three-dimensional CA for an AZ31 magnesium alloy. It was observed that the grain size increased as the temperature rose, while the grain size decreased with

time increments. Zhu et al. [29] conducted a review of CA methods to simulate the dynamic recrystallization process, detailing the physical mechanisms involved in dynamic recrystallization (DRX). Fuyong et al. [30] performed a three-dimensional CA model to determine the grain growth of a low-carbon, high-strength steel. The grain growth speed and grain growth curvature at different temperatures were calculated. Song et al. [31] simulated the dynamic recrystallization of a near-alpha TA15 alloy during the friction welding process, applying dislocation density as a critical variable. A good agreement was observed between the experimental and simulated final grain sizes.

In the present work, a CA model is developed to predict the microstructure changes in lap-joined Ti₆Al₄V during the friction welding process. The CA model enables accurate predictions of dynamically recrystallized grain size. The effects of processing parameters, such as rotational speed (800-1,200 rpm) and tool dimension characteristics, are evaluated. Microstructure characteristics and grain evolution have a significant influence on the mechanical and structural design of high-strength alloys.

2. Materials and procedures

2.1 Heat transfer model

The heat transfer during FSSW occurs between the rotating tool and the workpiece material. Figure 1 shows a schematic representation of the welding process. The basic steps of the FSSW include the immersion stage, holding stage and retraction. Figure 1a depicts the immersion stage, in which the tool rotates at a specified velocity while the working plates are fixed.

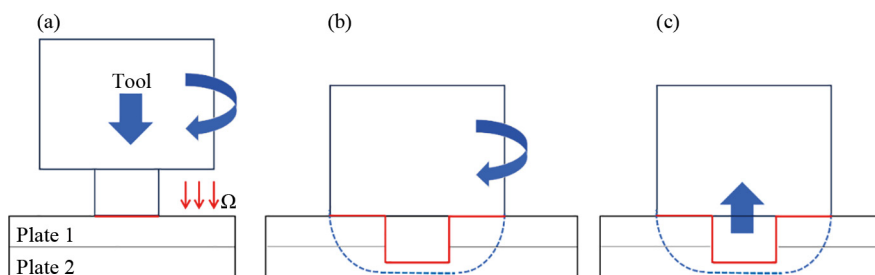


Figure 1. Schematic illustration of friction stir spot welding process, (a) immersion, (b) holding and (c) retraction

As the immersion stage starts, the tool begins to rotate and the pin contacts the surface of the top plate advancing at a specified distance. The deformation temperature is estimated based on Fourier's law:

$$\rho c \frac{dT}{dt} = \nabla(k \cdot \nabla T) + q\Omega, \quad (1)$$

where T is the temperature, k the thermal conductivity, c is the heat capacity, ρ is the density and q is the power [32]. After the immersion stage ends, a holding time is taken to generate the material consolidation. The heat generation from friction is expressed by:

$$dq = 2\pi wr^2 \mu(T) p(T) dr. \quad (2)$$

The heat generated between the contact interfaces is observed in Figure 1b, which can be expressed as:

$$\dot{q} = \int_{r_o}^{R_o} 2\pi\omega r^2 \mu(T)p(T)dr = \frac{2}{3}\pi\omega\mu(T)p(T)(R_o^3 - r_o^3). \quad (3)$$

The rate of heat generation is influenced by friction coefficient μ , the angular velocity ω and the tool radius r [18]. As the friction welding progresses, the temperature increases, while the friction coefficient starts to decrease. After the immersion stage finished, the tool is retracted as shown in Figure 1c. There is a dependence of temperature for the friction coefficient and the plastic flow. However, a constant value of friction coefficient is commonly defined to evaluate the thermal and plastic flow during friction welding.

2.2 Processing parameters

The Ti₆Al₄V alloy consists of $\alpha + \beta$ phases, which affect the thermal and mechanical evolution of the material. The principal elements of Ti₆Al₄V in weight percentage are presented in Table 1. In addition, Ti₆Al₄V presents different morphologies, which are associated with the heat and deformation state of the material.

Table 1. Composition of the Ti₆Al₄V (wt. %) [33]

| Al | V | Fe | O | N | C | Ti |
|------|------|------|------|-------|-------|---------|
| 6.38 | 4.07 | 0.19 | 0.17 | 0.008 | 0.012 | Balance |

The experiment evaluates the primary parameters of FSSW Ti₆Al₄V. The friction process consists in lap-weld thin square plates of 50 mm by 50 mm. The principal processing parameters are the rotational speed, the immersion depth and the tool material. A constant holding time of 2 s was defined during the process. Table 2 shows the selected values for the simulation of friction spot welding process.

Table 2. Parameters of friction spot welding of Ti₆Al₄V

| Test | Rotational speed (rpm) | Immersion depth (mm) | Tool material | Workpiece material |
|------|------------------------|----------------------|---------------|-----------------------------------|
| 1-5 | 800-1,200 | 4 | PCBN | Ti ₆ Al ₄ V |

The experiment consisted of five lap-welding simulations with variation of rotational speed from 800 to 1,200 rpm, with increments of 100 rpm. A thickness of 3 mm was considered for the upper and lower plates. The immersion depth of the tooling was defined as a constant parameter with a value of 4 mm. The experimental trails were performed using a Bridgeport high-speed machining center [33].

2.3 Finite element model

A finite element model was created to predict the thermal and mechanical response of lap-welding Ti₆Al₄V using a PCBN tool. The geometrical design consists of two thin plates lap-welded by a complex curved thread tool. The overlapping distance between plates was 18 mm and the assigned rotational velocity fluctuates from 800 to 1,200 rpm. The mechanical properties of Ti₆Al₄V were defined considering the plasticity and hardening effect of the material. The plastic flow was defined using a Johnson-Cook model [33]:

$$\sigma = \left[A + B(\bar{\epsilon}^{pl})^n \right] \left[1 + C \ln \frac{\bar{\epsilon}^{pl}}{\dot{\epsilon}_0^{pl}} \right] \left[\frac{T - T_{ambient}}{T_{melt} - T_{ambient}} \right] \quad (4)$$

The model calculates the nonlinearity associated with plastic deformation at high temperatures and strain rates. Table 3 includes the values for each parameter of the Johnson-Cook model.

The plastic flow of Ti₆Al₄V is strain rate sensitive due to the temperature increment during friction welding. As the temperature and strain increases during friction welding, dynamic recrystallization occurs. The heat capacity and thermal conductivity of the Ti₆Al₄V alloy is presented in Figure 2.

Table 3. Johnson-Cook parameters utilized in the friction welding simulation [33]

| Parameter | Value |
|---|------------------|
| Elastic limit, A (MPa) | 782.7 |
| Hardening modulus, B (MPa) | 498.4 |
| Plastic deformation sensitivity, n | 0.28 |
| Coefficient of plastic deformation, C | 0.028 |
| Temperature of melting, T_{melt} (°C) | 1,662 |
| Plastic deformation, $\bar{\epsilon}^{pl}$ | 1 |
| Standard deformation speed, $\dot{\epsilon}_0^{pl}$ | 1E ⁻⁵ |

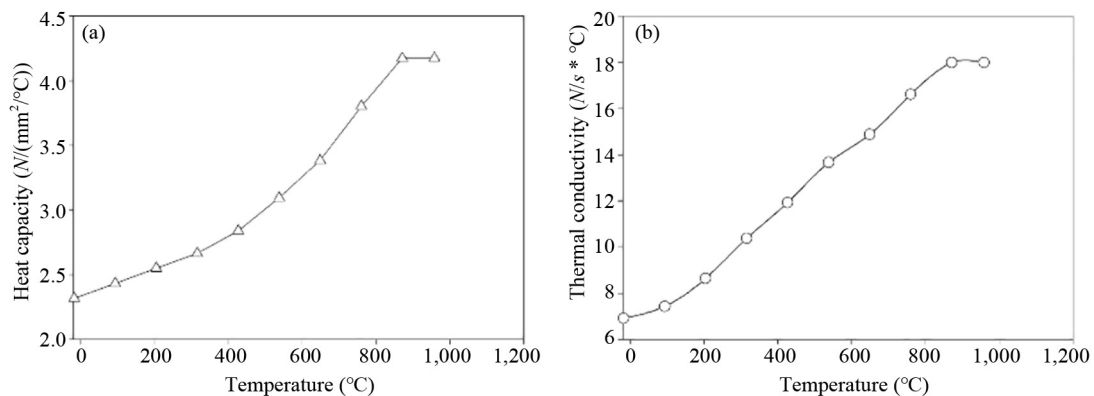


Figure 2. Thermal properties of Ti₆Al₄V alloy, (a) heat capacity and (b) thermal conductivity [4]

The Ti₆Al₄V plates were considered plastic materials, while the rotating tool and support plate were considered as rigid bodies. This condition decreases the computation time of the solution during the finite element simulation. A polycrystalline cubic boron nitride (PCBN) material was selected for the rotating tool. PCBN brings good wear properties, high thermal conductivity and hardness [34]. Figure 3 shows heat capacity and thermal conductivity of the tool's material.

The discretization procedure of the finite element model is shown in Figure 4. The mesh of the Ti₆Al₄V plates consisted of 7,915 nodes and 50,000 elements, see Figure 4a. The mesh of the rotating tool consisted of 16,321 nodes and 80,000 elements. During the friction welding process, the mesh gradually distorts, thus a re-mesh criterion was selected.

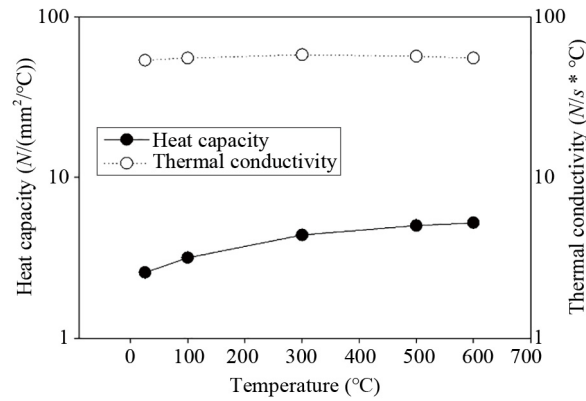


Figure 3. Thermal properties of PCBN tool [29]

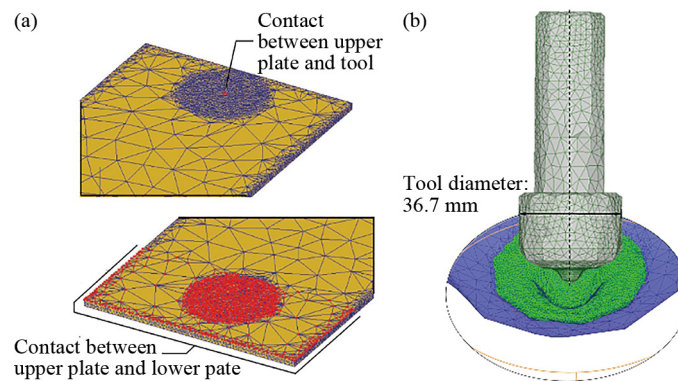


Figure 4. Finite element model of friction welding process, (a) upper and lower contact conditions and (b) discretization of the welding zone

As observed in Figure 4b, the complex curved thread tool consists of two concentric parts of different diameters, a larger diameter shoulder of 36.7 mm and a smaller diameter taper pin of 6 mm. In order to verify the finite element model, an experimental process based on previous work was followed [33]. The temperature profile of the weld nugget region was verified in the welding experiment.

3. Cellular automata model

As described in the previous section, the thermo-mechanical conditions were investigated by the finite element method. The microstructure evolution is dependent on the temperature and deformation of the friction process. The evolution of recrystallized grain size is analyzed using a cellular automata model. In the CA model, a regular pattern is defined by a group of equally shaped square cells with consistent boundaries. A certain grain number is stated in each unit cell, which indicates the state of recrystallization; when selecting a unit cell, the recrystallization and number of grains may cause the unit cell to change. When grains encounter nucleating conditions and selected neighbors recrystallize, their numbers shift to different values; this balances the number of its grains with those of its recrystallized neighbors, increasing the grain size [35].

A driving force must be specified to evaluate dynamic recrystallization; thus, dislocation density is considered as the driving force to DRX. Previous studies have shown that dislocation density presents an accurate effect on the kinetics of the material [36]. A regular lattice of 100 rows and 100 columns was specified in the CA model. The boundary condition in each unit cell considered the growth of surrounding nuclei. The spatial size of the model considers the radius of the

neighbors; this radius affects the grain size and controls the impact of the microstructure during the friction welding process. A function was selected based on dislocation density and nucleation probability due to the requirement of a critical dislocation density to nucleate new grains. The initial microstructure was created from grain boundaries and grain orientations with defined dislocation densities [37]. Figure 5 presents a diagram of the cellular automata procedure to determine the recrystallized grain size during friction welding.

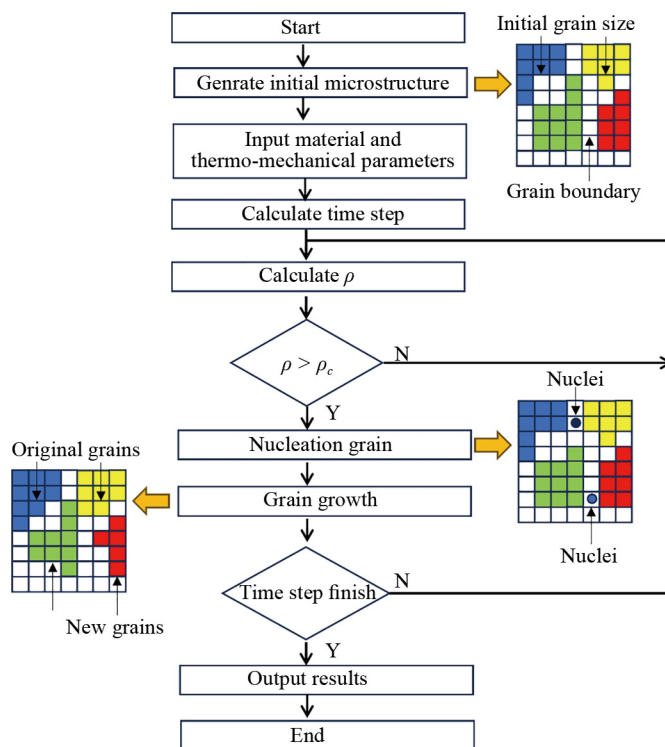


Figure 5. Diagram of cellular automata model for microstructure evolution of friction spot welded Ti₆Al₄V

3.1 Dislocation density model

The dislocation density represents the stored energy due to plastic flow of friction spot welding. A Laasraoui-Jonas model was considered to evaluate the microstructure in terms of dislocation density, recovery and hardening mechanisms [38]. The variation of dislocation density is expressed as follows:

$$d\rho_i = (h - r\rho_i)d\varepsilon - \rho_idV. \quad (5)$$

The phenomenological equation includes: a dislocation density ρ_i , the hardening h , a recovery term r , the strain ε and the volume across grain boundaries dV . The hardening and recovery terms also refer to temperature and strain rate conditions [39]. The coefficients for hardening and recovery can be calculated as follows:

$$h = h_0 \left(\frac{\dot{\varepsilon}}{\dot{\varepsilon}_0} \right) \exp \left(\frac{mQ}{RT} \right), \quad (6)$$

$$r = r_0 \left(\frac{\dot{\varepsilon}}{\dot{\varepsilon}_0} \right)^{-m} \exp \left(\frac{-mQ}{RT} \right). \quad (7)$$

The sensitivity to deformation is specified as m , Q is the activation energy, h_0 is a hardening constant and r_0 is the recovery constant. In order to calibrate strain ε_0 a value of 1 was considered [40]. The flow stress is related to the dislocation density as follows:

$$\sigma = M\alpha_1 Gb\sqrt{\rho}, \quad (8)$$

where M is the Taylor factor, b is the Burger's vector and G is the shear modulus. If Equation (5) is integrated and substituted in Equation (8):

$$\sigma = [\sigma_\infty^2 - (\sigma_\infty^2 - \sigma_e^2) \exp(-r\varepsilon)]^{1/2}. \quad (9)$$

Re-writing Equation (5) gives:

$$2\sigma \frac{d\sigma}{d\varepsilon} = r\sigma_\infty^2 - r\sigma^2. \quad (10)$$

According to Equation (10), the recovery term is defined as the slope $2\sigma \frac{d\sigma}{d\varepsilon}$ against σ^2 , while the h term is the crossing value with the perpendicular axis. Equation (11) evaluates the flow stress in terms of hardening and recovery coefficients.

$$\sigma_\infty = M\alpha_1 Gb\sqrt{\frac{h}{r}}. \quad (11)$$

Equations (6) and (7) can be used to calculate the coefficients h and r as functions of temperature and strain rate. The preceding equations must be added to consider an early dislocation density.

3.2 Nucleation model

During recrystallization the nucleation rate is proportional to the temperature and strain rate as follows [41]:

$$\dot{\eta} = C\dot{\varepsilon} \exp \left(-\frac{Q}{RT} \right), \quad (12)$$

where $\dot{\eta}$ is the nucleation rate and C is a constant. Commonly, nucleation occurs in the grain boundaries with a critical dislocation density defined as [42]:

$$\rho_{cd} = \left(\frac{20\gamma_i \dot{\epsilon}}{3blM\tau^2} \right)^{\frac{1}{3}}, \quad (13)$$

where τ is the dislocation line energy, M is the grain boundary mobility (defined as 0.5), l is the mean free path and γ_i the grain boundary energy. If the dislocation density reaches a critical value, the nucleus is set on the grain boundaries (see Figure 5).

The high angle grain boundary energy is determined by [43]:

$$\gamma_m = \frac{Gb\theta_m}{4\pi(1-\nu)}, \quad (14)$$

where γ_m is the high angle grain boundary energy and θ_m is the misorientation between high angle boundaries, G is the shear modulus and ν is the Poisson's ratio.

The dislocation mean free path is expressed as follows:

$$l = \frac{C_1 Gb}{\bar{\sigma}}, \quad (15)$$

where the constant C_1 is 10 for the most metals. The dislocation line energy τ is obtained by:

$$\tau = C_2 Gb^2, \quad (16)$$

where G is the shear modulus and C_2 is a constant. The grain boundary migration velocity v_0 is defined as $0.1 \mu\text{m/s}$, as previously reported [44]. In the simulation process, the cellular automata model randomly selects a given number of cells in each step based on:

$$N_r = \left(\frac{(\#rows)(\#columns)\sqrt{2}}{K} \right)^2 h(d\epsilon)^{(1-2m)}, \quad (17)$$

where N_r is the number of cells selected in the CA model and K is a constant with a value of 6,030. The parameters of the CA model for $\text{Ti}_6\text{Al}_4\text{V}$ are summarized in Table 4.

Table 4. Parameters in the CA model of $\text{Ti}_6\text{Al}_4\text{V}$ [44]

| G (MPa) | h_0 (μm^{-2}) | r | m | Q (kJ/mol) | v_0 ($\mu\text{m/s}$) | b (μm) | ϵ_0 (s^{-1}) |
|-----------|------------------------------|--------|-----|--------------|---------------------------|-----------------------|----------------------------------|
| 44,000 | 0.398 | 28,837 | 0.2 | 266,000 | 0.1 | 0.000286 | 1 |

The recovery and hardening coefficients were obtained from previous work based on experimental flow stress-strain curves of $\text{Ti}_6\text{Al}_4\text{V}$ [44]. Prior to the joining process, a dislocation density of $0.001 \mu\text{m}/\mu\text{m}^3$ was specified for the working material [45].

4. Results and discussion

4.1 Finite element results

This section presents the numerical results of lap-welded Ti₆Al₄V plates by friction spot welding process. The simulated maximum temperature reached at different rotational speeds (800-1,200 rpm) is observed in Figure 6.

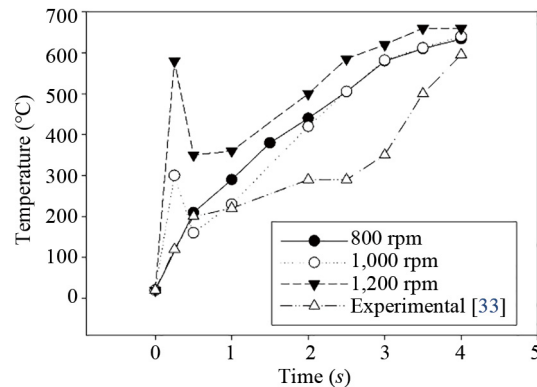


Figure 6. Finite element results of maximum temperature reached during friction welding at different rotational speeds

The results reveal significant findings regarding temperature distribution during friction spot welding. The analysis determined that the highest temperature, 678 °C, occurs in the stirring zone of the weld nugget. Notably, this peak temperature remains below the β transus temperature of approximately 900 °C across the various rotational speeds evaluated. This indicates that the welding process did not exceed the phase transformation threshold, which is crucial for controlling the microstructural properties of the alloy.

The study also highlighted the direct relationship between the generated heat and both the rotational speed and the physical characteristics of the tool, including the pin length, shape and shoulder diameter. The maximum temperature observed in the model was consistent with experimental findings reported by Quiroz et al. [33], where similar conditions were applied to friction spot weld thin plates of Ti₆Al₄V. Specifically, the highest temperature recorded was concentrated in the shoulder area of the tool, which aligns with experimental observations. Furthermore, the research found that the temperature near the tool and at the surface of the upper plate was effectively the same, indicating a uniform heat distribution at the interface, see Figure 7. This consistency supports the validity of the CA model in replicating real-world temperature profiles during the welding process, reinforcing its utility in predicting the microstructural evolution in titanium alloy joints.

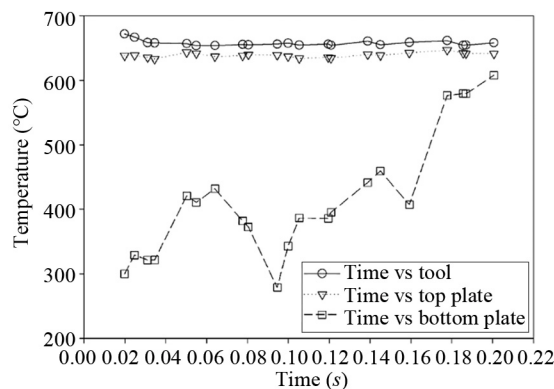


Figure 7. Maximum temperature recorded for top plate, bottom plate, and tool (800 rpm)

In addition, the maximum effective strain of the weld nugget was numerically evaluated; this region presents a greater plastic deformation in the contact zone between the tool and upper plate, see Figure 8. This high strain is crucial for understanding how mechanical forces during welding influence the microstructure and overall quality of the joint. The findings highlight the areas where the material undergoes the most intense deformation, shedding light on the relationship between the applied strain and resulting grain evolution. This insight helps improve the prediction and control of microstructural changes within titanium alloys, contributing to the optimization of welding processes for enhanced mechanical properties.

The results for the axial force during the welding process at a rotational speed of 800 rpm, as depicted in Figure 9, reveal key observations about the behavior of the Ti₆Al₄V alloy. Initially, the axial force reaches a significant peak of approximately 11,000 N. This peak occurs at the start of the welding process when the material is relatively harder and resists deformation. As the process progresses and the temperature around the tool pin rises, the alloy undergoes softening. This thermal effect reduces the resistance of the material, which facilitates the tool's penetration and results in a gradual reduction of the axial force. The softening behavior of the alloy supports a smoother downward pressure, enabling better interaction between the tool and the plates.

Different heat generation zones occurred during friction welding process, as observed in Figure 10. Two regions are indicated: a stir zone (SZ) and a heat affected zone (HAZ). These regions agree with the previous study by Nader et al. [46], in which FSSW of Ti₆Al₄V generated a stir zone and a heat affected zone with no evidence of transition region or thermo-mechanical affected zone.

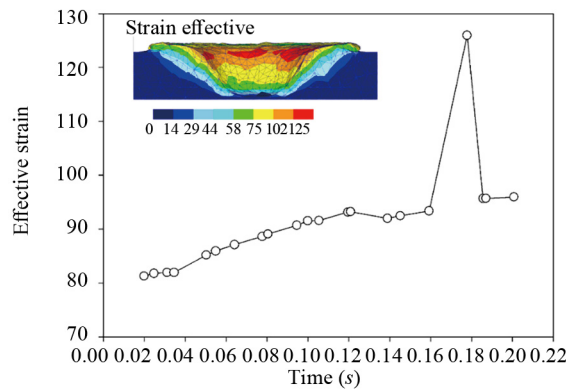


Figure 8. Maximum strain during friction spot welding at rotational speed of 800 rpm

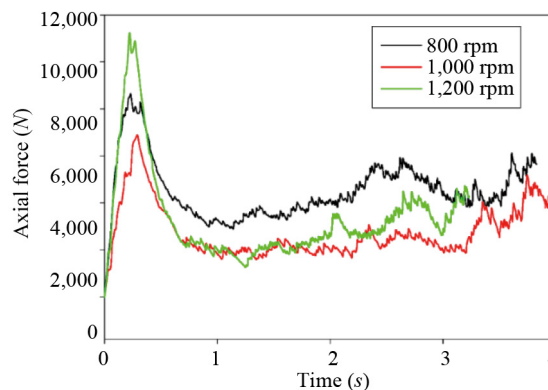


Figure 9. Numerical results of axial force during friction welding of Ti₆Al₄V plates at different rotational speeds

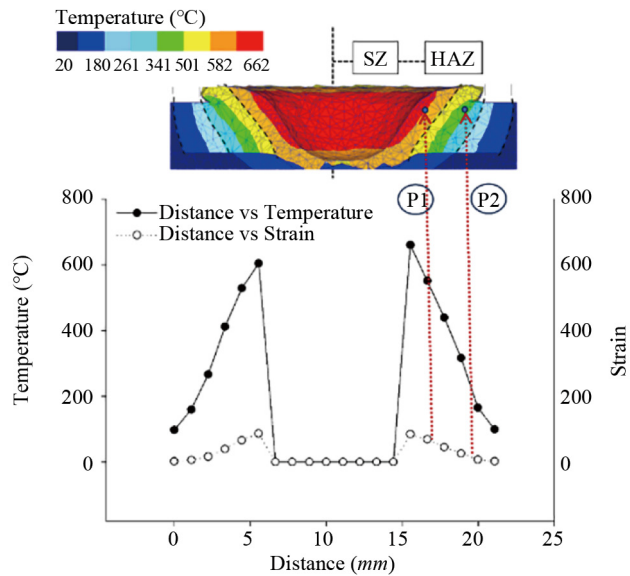


Figure 10. Numerical results of temperature and strain effective in the weld nugget at 1,000 rpm

The thermal evolution of the nugget zone is numerically simulated and an increase of temperature and strain due to frictional effect of the tool is observed. The heat generation is limited at the welding region, presenting a very narrow heat affected zone due to the low thermal properties of Ti_6Al_4V . Two points near the stir zone (P1) and the heat affected zone (P2) are selected to evaluate the thermo-mechanical evolution of the joint. The nugget presents a basin shape with a decrease of width on the weld base. The SZ of the weld nugget is where the greatest amount of heat is generated; the maximum recorded temperature was $662\text{ }^{\circ}\text{C}$. The adjacent zone corresponds to the heat affected zone, which registers temperatures from $255\text{ }^{\circ}\text{C}$ to $49\text{ }^{\circ}\text{C}$. The HAZ experiences a thermal effect that changes the grain size and the mechanical properties; however, there is a decrease of deformation in this zone. Similarly, it is possible to observe that the base material does not experience visible plastic deformation. The recorded temperature on the base material ranges from $20\text{ }^{\circ}\text{C}$ to $98\text{ }^{\circ}\text{C}$. Although, the maximum recorded temperature is below the β transus, the SZ exceeded the activation threshold of transformation from the $\alpha + \beta$ phase to the β phase, which begins around $600\text{ }^{\circ}\text{C}$. According to Buffa et al. [47], the SZ shows changes in its microstructure due to a combination of local plastic deformation and dynamic recrystallization mechanisms caused by the tool agitation; this condition exceeded the phase transformation initiation threshold. The lower rotational velocity decreases the peak temperature. The maximum temperatures are located at the central region of the stir zone. It is observed that, when the rotational speed increases from 800 to 1,200 rpm, there is a slight increase of temperature, and the maximum temperature is located at the external region of the nugget zone. Yue et al. [48] reported that a higher thermal effect is associated with tunnel defects in the joint. Thus, in the present work only rotational velocities of 800 and 1,000 rpm are considered for further analysis.

The point located in the stir zone (P1) presented a higher strain of 45 after the welding process, while the point P2 located near the HAZ presented a maximum effective strain of 29. The effective strain during the friction welding process is caused by the plastic flow between the workpiece and the tool. The larger strain is detected at the top of the nugget; this effect is associated with the tool shoulder interaction. According to Buffa et al. [47], the phase transformation is triggered by the coupled action of temperature and strain. As strain increases, the temperature for a full transformation decreases. In the following section, the discrete locations P1 and P2 are evaluated to predict the microstructure evolution after friction stir welding. This study correlates the effect of process parameters (temperature and strain) with the obtained grain size. The microstructure transformation is associated with the mechanical properties of the joint, which represents an important contribution to the expansion of knowledge regarding the interaction of Ti_6Al_4V and the used tool design in

the friction spot welding process. The results provide a deeper understanding of heat localization and distribution, which is essential for optimizing welding parameters and achieving desired mechanical properties in aerospace applications.

4.2 Cellular automata results

The results highlight the prediction of grain size evolution in the stirring zone (SZ) of a titanium alloy using a cellular automata model, see Figure 11. Initially, the model starts with an average grain size of $38 \mu\text{m}$ to represent the alloy's pre-welding microstructure. At the early stages of the process, a necklace structure of grains forms when the effective strain reaches approximately 42 mm/mm . As the welding process advances, this structure evolves and the grains undergo significant refinement, resulting in a final average grain size of $6.6 \mu\text{m}$. The model indicates a peak effective strain of 45 mm/mm during the process. In the SZ (location P1), the model reveals a partially transformed microstructure where fine recrystallized grains coexist with some coarse grains, indicating the dynamic nature of grain evolution. The study shows an initial accumulation of dislocation density due to strain hardening, which decreases as dynamic recrystallization (DRX) progresses and softening mechanisms take over. Notably, the untransformed microstructure observed confirms that the temperature in the SZ remains below the β transus. This aligns with the known behavior of titanium alloys, where temperatures below the β transus result in a microstructure composed of both α and β phases [49]. This finding corroborates that the welding process in this context does not reach the full transformation temperature required for a complete β phase structure, thus preserving a mixed-phase microstructure.

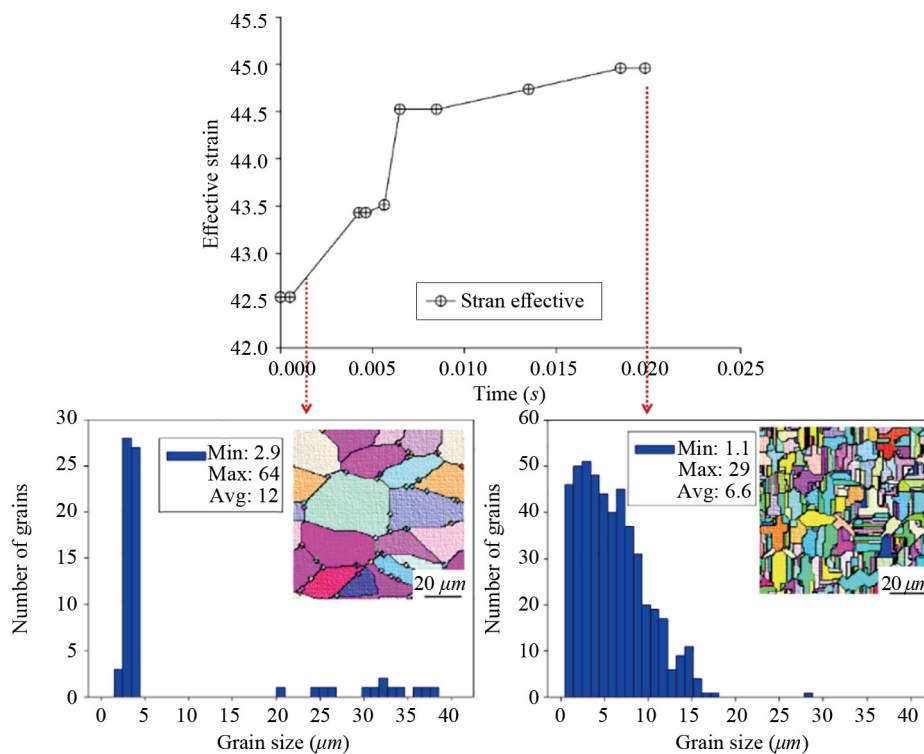


Figure 11. Cellular automata model for stir zone of lap-welded $\text{Ti}_6\text{Al}_4\text{V}$ at 800 rpm

The selected point P2 located in the HAZ presented an average grain size value of $6.3 \mu\text{m}$ and a maximum grain size of $23 \mu\text{m}$, see Figure 12. For the selected points, the dislocation density exceeds the critical condition, thus, nucleation and grain growth occur at the grain boundaries. After the friction welding process was completed, a significantly refined grain size was observed. The maximum effective strain for the HAZ was 29 mm/mm , which is lower than on the SZ.

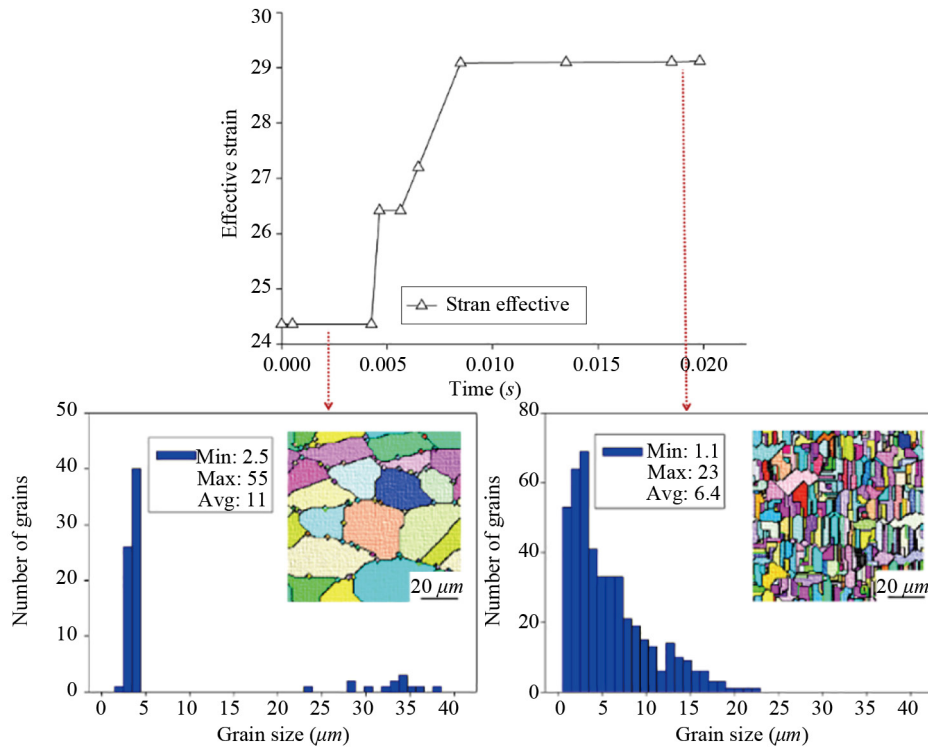


Figure 12. Cellular automata model for HAZ of lap-welded Ti_6Al_4V at 800 rpm

The average grain size of P1 was $6.6 \mu m$, while P2 presented an average grain value of $6.4 \mu m$. These results agree with previous work by Park [49] where an average grain size of $6.9 \mu m$ was reported in the weld center of thin plates of Ti_6Al_4V welded by pinless friction spot process. A refined grain size was obtained in the stir zone, where a correlation between thermo-mechanical process and microstructure evolution was verified. In addition, Fuji et al. [50] welded Ti alloy plates by FSW process. A maximum temperature below α/β transformation point was observed. The average grain size presented a value of $4 \mu m$ for a welding speed of 2.5 mm/s. Cellular automata results for welding process condition at 1,000 rpm are shown in Figure 13. Friction stir welding process generated a significant reduction of grain size which is associated with a dynamic recrystallization phenomenon [18].

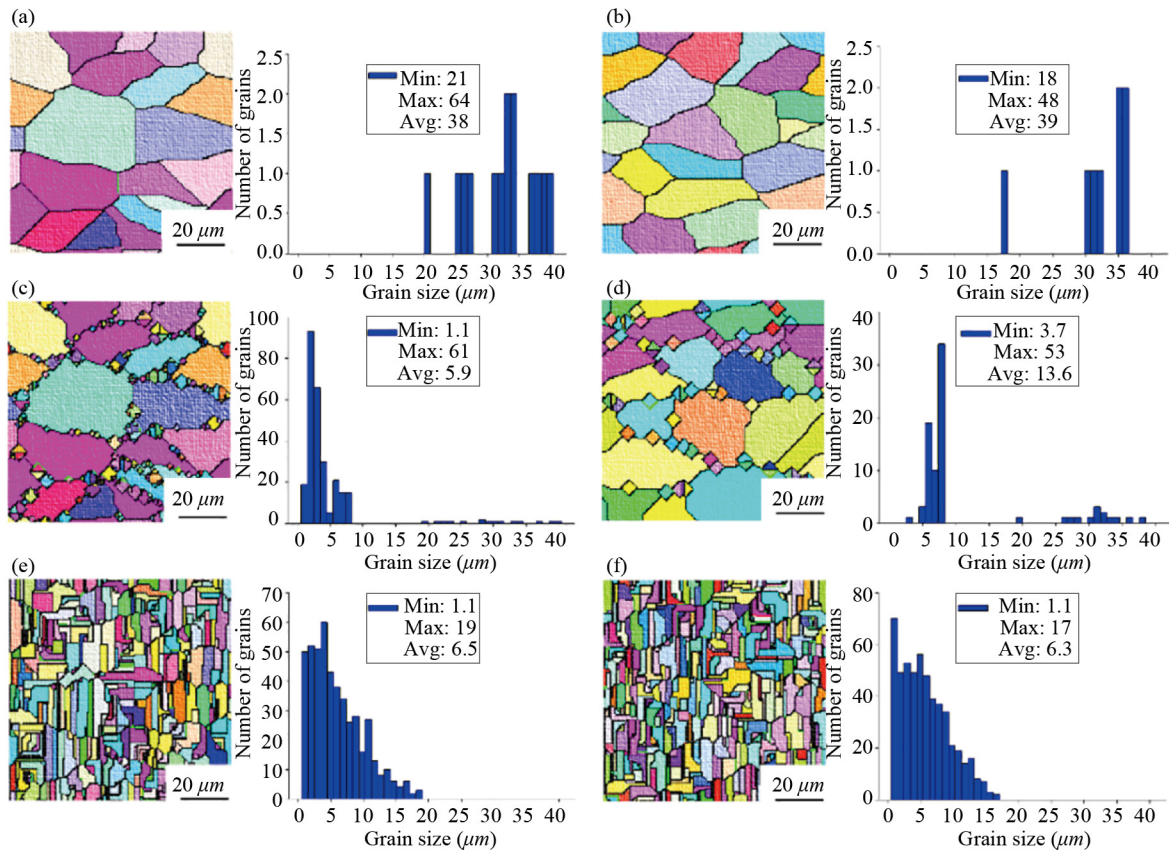


Figure 13. Cellular automata model of lap-welded Ti_6Al_4V at 1,000 rpm, (a) P1-SZ initial grain size, (b) P2-HAZ initial grain size, (c) P1-SZ transient recrystallized grain, (d) P2-HAZ transient recrystallized grain, (e) P1-SZ final grain size and (f) P2-HAZ final grain size

Figure 14 shows the misorientation angle vs. the number of grains of lap-welded Ti_6Al_4V plates for the SZ and HAZ. The misorientation angle distribution in the stir zone has a distinct effect compared to the base metal, which is associated with dynamic recrystallization. Misorientation angle was distributed from 2° to 62° . The largest peak was in the range of 38° to 48° for the SZ. As the temperature increases, the microstructure presents a reduction of α phase due to friction heating [49]. The strain conditions and dynamic recrystallization at high temperatures lead to defined grain size of Ti_6Al_4V alloy after friction welding process. Transformations of grain boundaries are a characteristic related to DRX.

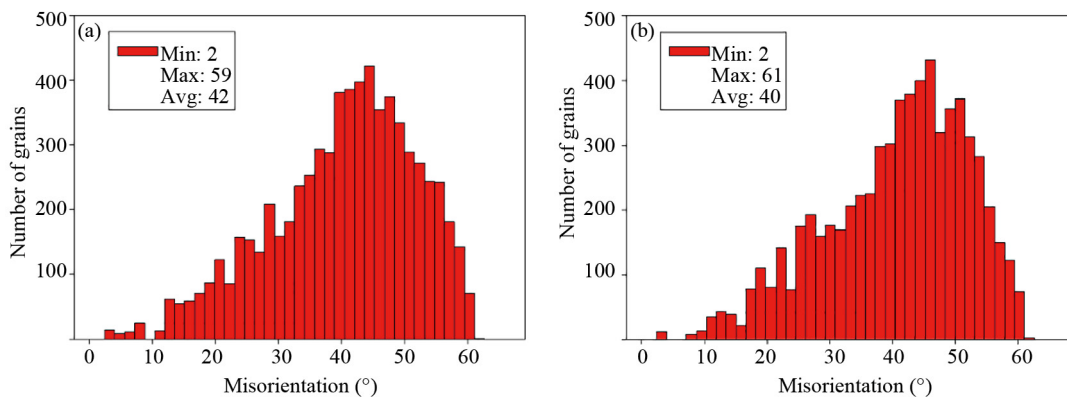


Figure 14. Misorientation angle vs. the number of grains of lap-welded Ti_6Al_4V at 1,000 rpm, (a) P1 SZ and (b) HAZ

The CA results of average grain size were compared with previous works of friction spot welded Ti₆Al₄V [46, 49]. The evolution of simulated grain size is observed in Figure 15, where the grain transforms from 38 μm for the base metal to 6.5 μm at the weld nugget. A steady mean grain size at the end of the process is observed. This effect is associated with the competition of hardening and recovery phenomena during DRX process. The CA model was validated with previous experimental grain size data for friction stir spot welding of Ti₆Al₄V [46, 49]. The simulated values of average grain size presented good agreement with experimental results. The deviation between simulated and experimental grain size was less than 0.5 μm for the lap-welded Ti₆Al₄V alloy.

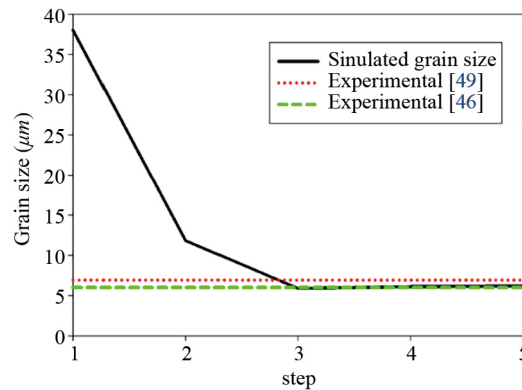


Figure 15. Cellular automata average grain size in the nugget zone for welding condition at 800 rpm

The microstructure in the weld zone showed a refined grain size which originated below the β transus temperature but above the activation threshold of transformation from the $\alpha + \beta$ phase to the β phase. The increase of volume fraction of phase is limited, consisting of nodular α with low portions of β phase [4]. In general, the hardness in the weld is higher than that of the parent metal as reported previously [47]. As the grain changes and the equilibrium condition for recrystallization processes is reached, friction welding process exhibits a rather stable grain size.

5. Conclusions

A numerical model was developed to predict the joining process of Ti₆Al₄V alloy by friction stir spot welding using a PCBN tool material. The principal conclusions drawn from this work are:

- The thermo-mechanical behavior of joined Ti₆Al₄V by FSSW was predicted.
- The results from the numerical study were compared with previously reported data showing good agreement. A maximum temperature below α/β transformation point was observed. However, it is possible to exceed the activation threshold of transformation from the $\alpha + \beta$ phase to the β phase, which starts around 600 °C.
- A CA model was developed to evaluate the grain size evolution of friction welding and a stable grain size was observed in the stir zone. The selected points (P1 and P2) presented full recrystallization and average grain size of around 6.5 μm .
- The predicted grain size using the CA technique showed good agreement. A grain size variation less than 0.5 μm was observed for the friction lap-welded Ti₆Al₄V alloy.
- The stir zone presented changes in the microstructure due to the combination of local plastic deformation, dynamic recrystallization and temperature.
- The greatest plastic deformation was recorded in the upper region of the nugget due to the greater contact between the shoulder of the tool and the workpiece.
- This work contributes to the knowledge of mechanical and microstructural evolution of FSSW processes.

Acknowledgments

This research work was supported by the Universidad Autonoma de Nuevo Leon.

Conflict of interest

The authors declared no potential conflicts of interest with respect to the research, authorship, and/or publication of this article.

References

- [1] Cui C, Hu BM, Zhao L, Liu S. Titanium alloy production technology, market prospects and industry development. *Materials and Design*. 2011; 32(3): 1684-1691. Available from: <https://doi.org/10.1016/j.matdes.2010.09.011>.
- [2] Zhan X, Liu Y, Liu J, Meng Y, Wei Y, Yang J, et al. Comparative study on experimental and numerical investigations of laser beam and electron beam welded joints for Ti₆Al₄V alloy. *Journal of Laser Applications*. 2017; 29: 012020. Available from: <https://doi.org/10.2351/1.4975824>.
- [3] Qi C, Zhan X, Gao Q, Liu L, Song Y, Li Y. The influence of the pre-placed powder layers on the morphology, microscopic characteristics and microhardness of Ti₆Al₄V/WC MMC coatings during laser cladding. *Optics and Laser Technology*. 2019; 119: 105572. Available from: <https://doi.org/10.1016/j.optlastec.2019.105572>.
- [4] Nu HTM, Le TT, Minh LP, Loc NH. A study on rotary friction welding of titanium alloy (Ti₆Al₄V). *Advances in Materials Science and Engineering*. 2019; 2019(1): 4728213. Available from: <https://doi.org/10.1155/2019/4728213>.
- [5] Chai P, Hu W, Ji S, Ai X, Lv Z, Song Q. Refill friction stir spot welding dissimilar Al/Mg alloys. *Journal of Materials Engineering and Performance*. 2019; 28: 6174-6181. Available from: <https://doi.org/10.1007/s11665-019-04359-7>.
- [6] Aval HJ. Microstructure and residual stress distributions in friction stir welding of dissimilar aluminium alloys. *Materials and Design*. 2015; 87: 405-413. Available from: <https://doi.org/10.1016/j.matdes.2015.08.050>.
- [7] Song X, Ke L, Xing L, Liu F, Huang C. Effect of plunge speeds on hook geometries and mechanical properties in friction stir spot welding of A6061-T6 sheets. *International Journal of Advanced Manufacturing Technology*. 2014; 71: 2003-2010. Available from: <https://doi.org/10.1007/s00170-014-5632-y>.
- [8] Bozkurt Y, Salman S, Çam G. Effect of welding parameters on lap shear tensile properties of dissimilar friction stir spot welded AA 5754-H22/2024-T3 joints. *Science and Technology of Welding and Joining*. 2013; 18(4): 337-345. Available from: <https://doi.org/10.1179/1362171813Y.0000000111>.
- [9] Trimble D, O'Donnell GE, Monaghan J. Characterisation of tool shape and rotational speed for increased speed during friction stir welding of AA2024-T3. *Journal of Manufacturing Processes*. 2015; 17: 141-150. <https://doi.org/10.1016/j.jmapro.2014.08.007>.
- [10] Heidarzadeh A, Saeid T. Correlation between process parameters, grain size and hardness of friction-stir-welded Cu-Zn alloys. *Rare Metals*. 2018; 37: 388-398. Available from: <https://doi.org/10.1007/s12598-016-0704-9>.
- [11] Liu H, Hu Y, Wang H, Du S, Sekulic DP. Stationary shoulder supporting and tilting pin penetrating friction stir welding. *Journal of Materials Processing Technology*. 2018; 255: 596-604. Available from: <https://doi.org/10.1016/j.jmatprotec.2018.01.010>.
- [12] Khodaverdizadeh H, Heidarzadeh A, Saeid T. Effect of tool pin profile on microstructure and mechanical properties of friction stir welded pure copper joints. *Materials and Design*. 2013; 45: 265-270. Available from: <https://doi.org/10.1016/j.matdes.2012.09.010>.
- [13] Elangovan K, Balasubramanian V. Influences of pin profile and rotational speed of the tool on the formation of friction stir processing zone in AA2219 aluminium alloy. *Materials Science and Engineering: A*. 2007; 459: 7-18. Available from: <https://doi.org/10.1016/j.msea.2006.12.124>.
- [14] Casalino G, Campanelli S, Mortello M. Influence of shoulder geometry and coating of the tool on the friction stir welding of aluminium alloy plates. *Procedia Engineering*. 2014; 69: 1541-1548. Available from: <https://doi.org/10.1016/j.proeng.2014.03.153>.

- [15] Arora A, De A, Debroy T. Toward optimum friction stir welding tool shoulder diameter. *Scripta Materialia*. 2011; 64: 9-12. Available from: <https://doi.org/10.1016/j.scriptamat.2010.08.052>.
- [16] Zahmatkesh B, Enayati MH. A novel approach for development of surface nanocomposite by friction stir processing. *Materials Science and Engineering: A*. 2010; 527: 6734-6740. Available from: <https://doi.org/10.1016/j.msea.2010.07.024>.
- [17] Venkatesh KM, Arivarsu M, Manikandan M, Arivazhagan N. Review on friction stir welding of steels. *Materials Today: Proceedings*. 2018; 5: 13227-13235. Available from: <https://doi.org/10.1016/j.matpr.2018.02.313>.
- [18] Sarikavak Y. An advanced modelling to improve the prediction of thermal distribution in friction stir welding (FSW) for difficult to weld materials. *Journal of the Brazilian Society of Mechanical Sciences and Engineering*. 2021; 43(1): 4. Available from: <https://doi.org/10.1007/s40430-020-02735-2>.
- [19] Su H, Wu CS, Pittner A, Rethmeier M. Thermal energy generation and distribution in friction stir welding of aluminum alloys. *Energy*. 2014; 77: 720-731. Available from: <https://doi.org/10.1016/j.energy.2014.09.045>.
- [20] Medhi T, Roy BS, Debbarma S, Saha SC. Thermal modelling and effect of process parameters in friction stir welding. *Materials Today: Proceedings*. 2015; 2(4-5): 3178-3187. Available from: <https://doi.org/10.1016/j.matpr.2015.07.112>.
- [21] Zhang Z, Liu YL, Chen JT. Effect of shoulder size on the temperature rise and the material deformation in friction stir welding. *International Journal of Advanced Manufacturing Technology*. 2009; 45: 889-895. Available from: <https://doi.org/10.1007/s00170-009-2034-7>.
- [22] Agarwal S, Mishra LN. Attributes of residual neural networks for modeling fractional differential equations. *Heliyon*. 2024; 10(19): e38332. Available from: <https://doi.org/10.1016/j.heliyon.2024.e38332>.
- [23] Bhat IA, Mishra LN, Mishra VN, Abdel-Aty M, Qasymeh M. A comprehensive analysis for weakly singular nonlinear functional Volterra integral equations using discretization techniques. *Alexandria Engineering Journal*. 2024; 104: 564-575. Available from: <https://doi.org/10.1016/j.aej.2024.08.017>.
- [24] Bhat IA, Mishra LN. A comparative study of discretization techniques for augmented Urysohn type nonlinear functional Volterra integral equations and their convergence analysis. *Applied Mathematics and Computation*. 2024; 470: 128555. Available from: <https://doi.org/10.1016/j.amc.2024.128555>.
- [25] Bhat IA, Mishra LN, Mishra VN, Tunç C, Tunç O. Precision and efficiency of an interpolation approach to weakly singular integral equations. *International Journal of Numerical Methods for Heat and Fluid Flow*. 2024; 34(3): 1479-1499. Available from: <https://doi.org/10.1108/HFF-09-2023-0553>.
- [26] Raabe D. Cellular automata in materials science with particular reference to recrystallization simulation. *Annual Review of Materials Science*. 2002; 32: 53-76. Available from: <https://doi.org/10.1146/annurev.matsci.32.090601.152855>.
- [27] Pourian MH, Pilvin P, Bridier F, Bocher P. Modeling the elastoplastic behaviors of alpha Ti-alloys microstructure using Cellular Automaton and finite element methods. *Computational Materials Science*. 2015; 99: 33-42. Available from: <https://doi.org/10.1016/j.commatsci.2014.11.027>.
- [28] Li Y, Liu C, Chu Z, Li W, Wu Z, Gao S, et al. Grain growth of AZ31 magnesium alloy based on three-dimensional cellular automata. *Advances in Materials Science and Engineering*. 2020; 2020(1): 7615643. <https://doi.org/10.1155/2020/7615643>.
- [29] Zhu HJ, Chen F, Zhang HM, Cui ZS. Review on modeling and simulation of microstructure evolution during dynamic recrystallization using cellular automaton method. *Science China Technological Sciences*. 2020; 63(3): 357-396. Available from: <https://doi.org/10.1007/s11431-019-9548-x>.
- [30] Su F, Liu W, Wen Z. Three-dimensional cellular automaton simulation of austenite grain growth of $Fe_{1.5}Cr$ alloy steel. *Journal of Materials Research and Technology*. 2020; 9(1): 180-187. Available from: <https://doi.org/10.1016/j.jmrt.2019.10.043>.
- [31] Song KJ, Dong ZB, Fang K, Zhan XH, Wei YH. Cellular automaton modelling of dynamic recrystallisation microstructure evolution during friction stir welding of titanium alloy. *Materials Science and Technology*. 2014; 30(6): 700-711. Available from: <https://doi.org/10.1179/1743284713Y.0000000389>.
- [32] Chen CM, Kovacevic R. Finite element modeling of friction stir welding-thermal and thermomechanical analysis. *International Journal of Machine Tools and Manufacture*. 2003; 43(13): 1319-1326. [https://doi.org/10.1016/S0890-6955\(03\)00158-5](https://doi.org/10.1016/S0890-6955(03)00158-5).
- [33] Quiroz F, García-Castillo FA, Reyes-Osorio LA, Ávila-Cabrera A. Finite element modeling of friction stir spot welding (FSSW) of Ti_6Al_4V . *Proceedings of the Symposium on Aeronautical and Aerospace Processing of Materials*

for Industrial Applications. Switzerland: Springer Cham; 2017. Available from: https://doi.org/10.1007/978-3-319-65611-3_11.

- [34] García-Castillo FA, Reyes LA, Garza C, López-Botello OE, Hernández-Muñoz GM, Zambrano-Robledo P. Investigation of microstructure, mechanical properties, and numerical modeling of Ti₆Al₄V joints produced by friction stir spot welding. *Journal of Materials Engineering and Performance*. 2020; 29: 4105-4116. Available from: <https://doi.org/10.1007/s11665-020-04900-z>.
- [35] Jin ZY, Liu J, Cui ZS, Wei DL. Identification of nucleation parameter for cellular automaton model of dynamic recrystallization. *Transactions of Nonferrous Metals Society of China*. 2010; 20(3): 458-464. Available from: [https://doi.org/10.1016/S1003-6326\(09\)60162-X](https://doi.org/10.1016/S1003-6326(09)60162-X).
- [36] Janssens KGF. An introductory review of cellular automata modeling of moving grain boundaries in polycrystalline materials. *Mathematics and Computers in Simulation*. 2010; 80(7): 1361-1381. Available from: <https://doi.org/10.1016/j.matcom.2009.02.011>.
- [37] Liu C, Dong HB. Cellular automaton simulation of dynamic recrystallization for TC4-DT titanium alloy in β hot process. *Journal of Aeronautical Materials*. 2015; 35(2): 21-27. Available from: <https://doi.org/10.11868/j.issn.1005-5053.2015.2.003>.
- [38] Laasraoui A, Jonas JJ. Prediction of steel flow stresses at high temperatures and strain rates. *Metallurgical Transactions A*. 1991; 22: 1545-1558. Available from: <https://doi.org/10.1007/BF02667368>.
- [39] Iqbal MP, Tripathi A, Jain R, Mahto RP, Pal SK, Mandal P. Numerical modelling of microstructure in friction stir welding of aluminium alloys. *International Journal of Mechanical Sciences*. 2020; 185: 105882. Available from: <https://doi.org/10.1016/j.ijmecsci.2020.105882>.
- [40] Thomas JP, Montheillet F, Semiatin SL. Modeling of microstructure evolution during the thermomechanical processing of nickel-base superalloys. In *Fundamentals of Modeling for Metals Processing*. USA: ASM International; 2018. Available from: <https://doi.org/10.31399/asm.hb.v22a.a0005459>.
- [41] Qian M, Guo ZX. Cellular automata simulation of microstructural evolution during dynamic recrystallization of an HY-100 steel. *Materials Science and Engineering: A*. 2004; 365(1-2): 180-185. <https://doi.org/10.1016/j.msea.2003.09.025>.
- [42] Asadi P, Givi MKB, Akbari M. Microstructural simulation of friction stir welding using a cellular automaton method: A microstructure prediction of AZ91 magnesium alloy. *International Journal of Mechanical and Materials Engineering*. 2015; 10(20): 1-14. Available from: <https://doi.org/10.1186/s40712-015-0048-5>.
- [43] Xiao N, Zheng C, Li D, Li Y. A simulation of dynamic recrystallization by coupling a cellular automaton method with a topology deformation technique. *Computational Materials Science*. 2008; 41(3): 366-374. Available from: <https://doi.org/10.1016/j.commatsci.2007.04.021>.
- [44] Hu J, Yang S, Shuai Z, Wang X, Xu H. Microstructure study on large-sized Ti₆Al₄V bar three-high skew rolling based on cellular automaton model. *Metals*. 2022; 12(5): 773. Available from: <https://doi.org/10.3390/met12050773>.
- [45] Gourdet S, Montheillet F. A model of continuous dynamic recrystallization. *Acta Materialia*. 2003; 51(9): 2685-2699. [https://doi.org/10.1016/S1359-6454\(03\)00078-8](https://doi.org/10.1016/S1359-6454(03)00078-8).
- [46] Nader S, Kasiri-Asgarani M, Amini K, Shamanian M. Effect of welding parameters on microstructure and mechanical properties of friction stir spot welded of titanium alloy TiAl₆V₄. *International Journal of Advanced Design and Manufacturing Technology*. 2016; 9(2): 93-100.
- [47] Buffa G, Fratini L, Schneider M, Merklein M. Micro and macro mechanical characterization of friction stir welded Ti₆Al₄V lap joints through experiments and numerical simulation. *Journal of Materials Processing Technology*. 2013; 213(12): 2312-2322. Available from: <https://doi.org/10.1016/j.jmatprotec.2013.07.003>.
- [48] Yue Y, Wen Q, Ji S, Ma L, Lv Z. Effect of temperature field on formation of friction stir welding joints of Ti₆Al₄V titanium alloy. *High Temperature Materials and Processes*. 2017; 36(7): 733-739. Available from: <https://doi.org/10.1515/htmp-2015-0178>.
- [49] Park H. *Pinless Friction Stir Spot Welding of Ti₆Al₄V Alloy for Aerospace Application*. Knoxville, TN, USA: University of Tennessee; 2022.
- [50] Fujii H, Sun Y, Kato H, Nakata K. Investigation of welding parameter dependent microstructure and mechanical properties in friction stir welded pure Ti joints. *Materials Science and Engineering: A*. 2010; 527(15): 3386-3391. Available from: <https://doi.org/10.1016/j.msea.2010.02.023>.